Accelerator mass spectrometry measurements of the C-13(n,gamma)C-14 and N-14(n,p)C-14 cross sections

PHYSICAL REVIEW C **93**, 045803 (2016)

Accelerator mass spectrometry measurements of the $^{13}C(n,\gamma)^{14}C$ and $^{14}N(n,p)^{14}C$ cross sections

A. Wallner,[1,*] M. Bichler,[2] K. Buczak,[3] I. Dillmann,[4,†] F. Käppeler,[4] A. Karakas,[5] C. Lederer,[3,‡] M. Lugaro,[6] K. Mair,[3] A. Mengoni,[7] G. Schätzel,[3] P. Steier,[3] and H. P. Trautvetter[8]

[1]*Department of Nuclear Physics, Research School of Physics and Engineering, The Australian National University, 2601, Canberra, Australia and VERA Laboratory, University of Vienna, A-1090 Vienna, Austria*

[2]*Atominstitut, Vienna University of Technology, A-1020 Vienna, Austria*

[3]*VERA Laboratory, University of Vienna, A-1090 Vienna, Austria*

[4]*Karlsruhe Institute of Technology (KIT), Campus North, Institute of Nuclear Physics, PO Box 3640, D-76021 Karlsruhe, Germany*

[5]*School of Astronomy & Astrophysics, Mt. Stromlo Observatory, Australian National University, Canberra, Australia*

[6]*Konkoly Observatory, Hungarian Academy of Sciences, Hungary*

[7]*CERN, CH-1211 Geneva 23, Switzerland*

[8]*Ruhr University Bochum, D-44801 Bochum, Germany*

(Received 1 November 2015; published 11 April 2016)

The technique of accelerator mass spectrometry (AMS), offering a complementary tool for sensitive studies of key reactions in nuclear astrophysics, was applied for measurements of the $^{13}C(n,\gamma)^{14}C$ and the $^{14}N(n,p)^{14}C$ cross sections, which act as a neutron poison in *s*-process nucleosynthesis. Solid samples were irradiated at Karlsruhe Institute of Technology with neutrons closely resembling a Maxwell-Boltzmann distribution for $kT = 25$ keV, and also at higher energies between $E_n = 123$ and 182 keV. After neutron irradiation the produced amount of ^{14}C in the samples was measured by AMS at the Vienna Environmental Research Accelerator (VERA) facility. For both reactions the present results provide important improvements compared to previous experimental data, which were strongly discordant in the astrophysically relevant energy range and missing for the comparably strong resonances above 100 keV. For $^{13}C(n,\gamma)$ we find a four times smaller cross section around $kT = 25$ keV than a previous measurement. For $^{14}N(n,p)$, the present data suggest two times lower cross sections between 100 and 200 keV than had been obtained in previous experiments and data evaluations. The effect of the new stellar cross sections on the *s* process in low-mass asymptotic giant branch stars was studied for stellar models of 2 $M_\odot$ initial mass, and solar and $1/10^{\text{th}}$ solar metallicity.

DOI: 10.1103/PhysRevC.93.045803

I. INTRODUCTION

Half of the elemental abundances of the heavy elements are built by the slow neutron capture process (*s* process). As only moderate neutron densities are reached during stellar evolution, neutron capture rates are of the order of several months to years, much lower than typical β decay rates, thus restricting the *s*-process reaction path essentially to a sequence of (n,γ) reactions and β^- decays along the stability valley. Accordingly, neutron cross sections are the key nuclear physics input for any quantitative *s*-process model.

Stellar *s*-process scenarios are related to the He burning phases in massive stars and in thermally pulsing low-mass asymptotic giant branch (AGB) stars. Of special interest in the context of this work is the so-called *main s* component associated with AGB stars, where the $^{13}C(\alpha,n)$ reaction constitutes the dominant neutron source, whereas the *weak s* process in massive stars is driven by the $^{22}Ne(\alpha,n)$ source. Because of their lower neutron to seed ratio massive stars contribute mostly to the mass region from Fe to Sr, whereas AGB stars are mainly responsible for the *s* abundances between Zr and the Pb/Bi region. Important differences refer also to the respective temperature regimes, which are determining the burning conditions and the strength of neutron densities and neutron exposures (for more details, see [1,2] and references therein).

A. Main *s* process and the ^{13}C pocket in AGB stars

When AGB stars reach their final evolutionary stage, the core consists of inert C and O, and the stellar energy is now produced by the alternating activation of long H burning and comparably short He burning phases. This situation is sketched in Fig. 1. The high-energy release during the short He shell burning periods gives rise to thermal instabilities with strong convection and mixing. The temperature at the bottom of these He shell flashes rises to up to ~250 MK ($T_8 \sim 2.5$), sufficient for neutron production via $^{22}Ne(\alpha,n)$ reactions. Although peak neutron densities around 10^{10} cm^{-3} are reached in this way, the He shell flashes contribute only about 5% to the total neutron budget in AGBs. After each thermal instability the convective envelope can sink deep into the He-rich intershell, dredging up to the stellar surface the products of He burning (such as ^{12}C) and of the *s* process.

*anton.wallner@anu.edu.au

†Present address: TRIUMF, Vancouver BC, Canada.

‡Present address: University of Edinburgh, UK.

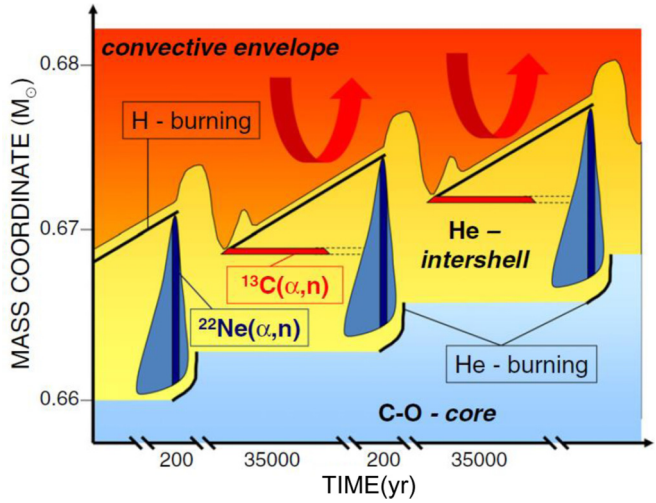

FIG. 1. Energy production and related *s*-process sites in thermally pulsing low-mass AGB stars are associated with recurrent H and He burning episodes. Short highly convective thermal instabilities during He shell flashes are separated by long radiative phases of H burning.

During the subsequent long phases of H burning the larger part of the neutron exposure is produced via ^{13}C(α,n) reactions in the so-called "^{13}C pocket" when a certain amount of H may mix from the envelope into the He intershell at the deepest extent of each dredge-up episode. The ^{13}C pocket consists of a thin layer as shown in Fig. 1 that forms after an He shell flash, when a certain amount of H is mixed from the envelope into the He intershell. These protons are captured by the ^{12}C admixture in the intershell leading to the reaction sequence ^{12}C$(p,\gamma)\,^{13}$N$(\beta^+)^{13}$C. The exact way the ^{13}C pocket is formed is complicated and still affected by persistent uncertainties as summarized in [1]. For practical reasons, a parametrized form was initiated by Gallino *et al.* [3] that was essentially guided by the observed *s* abundances. Only recently, there have been attempts to describe the formation of the ^{13}C pocket on the basis of realistic stellar physics [4–6].

B. New study of ^{13}C(n,γ) and ^{14}N(n,p) via activation and atom counting of the product ^{14}C

An important aspect of the ^{13}C pocket comes from the simultaneous formation of ^{14}N via ^{13}C$(p,\gamma)\,^{14}$N reactions. Note that both ^{13}C and ^{14}N are of primary origin, i.e., produced by the star itself independent of the initial metallicity. ^{14}N represents a significant neutron poison because of its large (n,p) cross section. So far, this reaction as well as the ^{13}C(n,γ) reaction are poorly known. Therefore, activation studies were performed using well-defined neutron fields and subsequent accelerator mass spectrometry (AMS) for sensitive cross section measurements for the ^{13}C(n,γ) channel, targeting discrepancies at $kT = 25$ keV between the two existing experiments [7,8] and theoretical work [9]. We also provide first experimental results at higher energies as well as improve the information on the ^{14}N(n,p) reaction.

In the astrophysically relevant keV neutron energy range, the (n,γ) cross sections of the light elements are usually of the order of some 10–100 μbarn, about 100–1000 times smaller than in the *s*-process domain between Fe and the Pb/Bi region. Nevertheless, they may constitute significant neutron poisons because a small capture cross section can be compensated by a very high abundance as in case of the ^{13}C and ^{14}N content of the pocket. While ^{12}C$(n,\gamma)^{13}$C reactions are also competing for neutrons, the produced ^{13}C will then act as a target for the ^{13}C$(\alpha,n)\,^{16}$O reaction so that the neutrons consumed by capture on ^{12}C are recycled, and thus recovered for the *s*-process budget [10]. On the contrary, the ^{13}C(n,γ) reaction hampers the production of neutrons not only in the manner of a usual poison, because the captured neutrons are lost for the *s* process, but also because primary ^{13}C target nuclei are transformed into long-lived ^{14}C.

The second reaction studied, ^{14}N$(n,p)^{14}$C, has a considerably higher cross section of ∼2 mb at keV energies because of the larger phase space in the exit channel. ^{14}N has an additional poisoning effect weakening the neutron source: The protons produced in the ^{14}N(n,p) reactions remove ^{13}C via (p,γ) reactions as in the CNO cycle. As a consequence, the constituents ^{14}N, ^{13}C, neutrons, and protons, form a reaction cycle with the end product being again ^{14}N. As such, this reaction represents the most important neutron poison in *s*-process nucleosynthesis.

An overview of the main reactions concerning neutron production and neutron poisons in the ^{13}C pocket is given in Fig. 2.

We investigated both reactions in the energy range around $kT = 25$ keV (simulating a Maxwell-Boltzmann distribution) and at two higher energies around $E_n = 125$ and 180 keV. These studies were complemented by measurements at thermal neutron energies for constraining the *s*-wave direct capture (DC) component of the cross section, which decreases with $1/v_n$ and is still important at keV energies in both cases. In the experiment, the irradiations with thermal and keV neutrons were performed at the TRIGA research reactor of the Atominstitut (ATI) in Vienna and at the 3.7 MV Van de Graaff (VdG) accelerator of the Karlsruhe Institute of Technology, respectively. After neutron activation the irradiated samples were subsequently analyzed at the AMS facility VERA. In this approach the produced ^{14}C atoms in the sample are directly counted rather than measuring the associated γ radiation or the protons emitted during the irradiation.

The present status of both reactions is summarized in Sec. II. Section III describes the sample material used. The

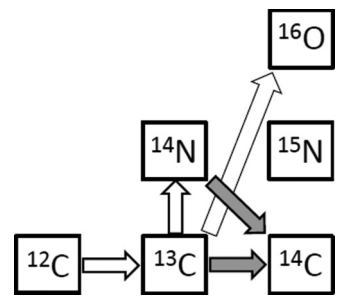

FIG. 2. The *s*-process network in the ^{13}C pocket for the main reactions among the CNO isotopes (the investigated cases are indicated by full arrows).

neutron irradiations and the AMS measurements are described in Secs. IV and V, followed by the data analysis and the results, which are presented in Sec. VI. The final Maxwellian averaged cross sections (MACS) are calculated in Sec. VII and compared with the values derived from evaluated cross sections and with the KADoNiS compilation [11,12]. The impact of the new MACS results on the *s* process in thermally pulsing low-mass asymptotic giant branch (AGB) stars is discussed in Sec. VIII.

II. EXISTING DATA

A. $^{13}C(n,\gamma)^{14}C$

The cross section of this reaction is determined by the interplay of *s*- and *p*-wave DC contributions with the tail of a pronounced capture resonance at E_n= 143 keV. Experimental data in the keV region are scarce for this reaction. First results by Raman *et al.* [7] were consolidated by Shima *et al.* [8], providing values for E_n = 25.1, 40, and 61.1 keV (see also Fig. 7). At higher energies the cross section is dominated by a resonance at E_n = 143 keV, of which only the neutron width is known so far. Possible interference effects with the *p*-wave DC component could therefore affect the cross section at astrophysical energies as well. Calculations by Herndl *et al.* [9] suggest that the reaction rate is essentially determined by the 143-keV resonance at temperatures above $T_8 \sim 3$, whereas the *s*- and *p*-wave DC contributions are dominating below. Nevertheless, the predicted energy dependence in [9] is in conflict with the experimental data around 30 keV. This discrepancy and the uncertain capture strength of the 143-keV resonance motivated the present work to extend the investigated energy range beyond the astrophysically important region to include the two data points at and slightly above the 143-keV resonance.

B. $^{14}N(n,p)^{14}C$

Much more work exists for $^{14}N(n,p)^{14}C$ in the keV energy range [13–16], The measurements by Koehler and O'Brien [14] support a 1/v energy dependence almost up to 100 keV. Above that energy the cross section is determined by the tails of two resonances at 493 and 655 keV. Between 10 and 200 keV most experimental data are in good agreement, except for the values by Brehm *et al.* [13], which are approximately two to three times lower (see also Fig. 6). This difference would have stringent consequences for the role of ^{14}N as a neutron poison as well as for the production of ^{19}F, which depends on the amount of protons emitted in the $^{14}N(n,p)$ reactions. While the ^{19}F abundance is not much affected by the 10% uncertainty of most experimental cross sections, this becomes a critical issue if one includes the data of Brehm *et al.* [17,18]. There are also large discrepancies between the evaluated $^{14}N(n,p)$ cross sections in the JEFF-3.1, ENDF/B-VII, JENDL, and BROND libraries, especially above about 50 keV.

Accordingly, the present measurements on ^{14}N were performed at the same neutron energies as for ^{13}C, in particular with respect to the discrepancies between existing experimental data and evaluated cross sections.

TABLE I. $^{14}C/^{13}C$ ratios and the corresponding production cross section for ^{14}C measured by irradiation of enriched ^{13}C-graphite samples with thermal neutrons.

Sample	Neutron fluence (10^{15} cm^{-2})	$^{14}C/^{13}C$ (10^{-11}at/at)	σ_{prod}[a] (mb)
C13-1	0.241 ± 0.010	0.25 ± 0.02	10.4 ± 1.0
C13-2	14.9 ± 0.7	1.60 ± 0.10	10.7 ± 0.9
C13-3	130 ± 10	13.5 ± 1.0	10.4 ± 0.9
Mean			10.5 ± 0.6

[a]Accounting for ^{14}C produced from both reactions, $^{13}C(n,\gamma)$, σ = 1.37 mb and $^{14}N(n,p)$, σ = 1860 mb.

III. SAMPLES

With natural carbon (~99% ^{12}C, ~1% ^{13}C) it is difficult to reach a significant ^{14}C signal above the present background levels achievable in AMS. Therefore, the $^{13}C(n,\gamma)$ reaction was studied with samples of ^{13}C-enriched graphite (98% ^{13}C) from AMT Ltd., Israel.

A general complication in measurements of the $^{13}C(n,\gamma)$ cross sections is that even spurious contents of ^{14}N in the sample material also produce significant amounts of ^{14}C via the $^{14}N(n,p)$ reaction, owing to its much higher cross section as illustrated in Table IV.

In view of this problem, the ^{14}N content of the ^{13}C-enriched graphite was characterized by two different methods:

(i) Using the AMS technique, $^{14}N\,^{13}C$ molecules from the ion source were injected into the tandem accelerator. After the molecular ions were decomposed in the terminal stripper, magnetic selection of mass 14 yielded directly the ^{14}N content in the beam.

(ii) The ^{13}C-enriched samples were irradiated at the TRIGA reactor in a thermal flux of 4×10^{11} s^{-1}cm^{-2}. Because the cross section ratio $\sigma_{np}/\sigma_{n\gamma}$ is highest at thermal energies (Table IV) and because the thermal cross sections of both reactions are well known, the parasitic ^{14}C production through the $^{14}N(n,p)$ channel could be studied with high sensitivity. The results of the thermal irradiations of ^{13}C-enriched graphite are summarized in Table I. From the measured effective thermal cross section, σ_{prod} [the sum of ^{14}C production from $^{13}C(n,\gamma)$ and $^{14}N(n,p)$], the intrinsic ^{14}N content in the graphite samples was then determined using the thermal cross section values for $^{13}C(n,\gamma)$ and $^{14}N(n,p)$ as outlined in Sec. VI B 2.

The samples for studying the $^{14}N(n,p)^{14}C$ reaction were prepared from uracil ($C_4H_4N_2O_2$). Owing to the low $^{13}C(n,\gamma)$ cross section and to the low ^{13}C abundance any parasitic ^{14}C production from neutron capture on ^{13}C was negligible (less than 0.35%).

IV. NEUTRON ACTIVATIONS AT keV ENERGIES

At the Karlsruhe VdG accelerator neutrons in the keV energy range were produced via the $^{7}Li(p,n)^{7}Be$ reaction by protons impinging on a Li target. Selecting the proton energy at 1912 keV, 31 keV above the reaction threshold, generates

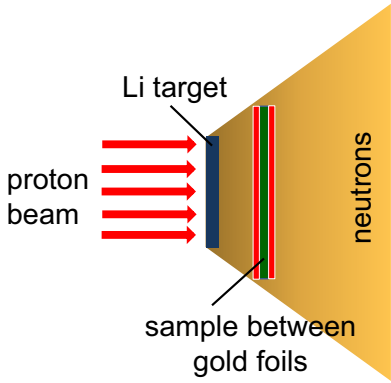

FIG. 3. Schematic sketch of the setup used for the activations at the Karlsuhe Van de Graaff.

a broad neutron spectrum in a forward cone according to kinematics and energy loss in the Li target. The corresponding setup at the Karlsuhe VdG accelerator is sketched in Fig. 3, illustrating the incoming proton beam, the conical neutron field emerging from the Li target, and the irradiated sample sandwich in close geometry to the neutron source. As the angle-integrated spectrum represents a good approximation of the true stellar neutron spectrum for a thermal energy of $kT = 25$ keV (Fig. 4), measurements in this quasi-Maxwell-Boltzmann (q-MB) spectrum are yielding MACS values for an effective thermal energy of $kT = 25$ keV with very little corrections [20,21].

The Li targets were produced by evaporation onto 1-mm thick windows of Faraday cups mounted at the end of the proton beam line. In the evaporation process, the thickness of the Li layers was determined with a calibrated oscillating quartz monitor.

For the $^{13}C(n,\gamma)^{14}C$ activations, samples were prepared from ^{13}C-enriched graphite powder. The powder was enclosed in small Al containers 6 mm in diameter. Gold foils served as monitors for the neutron fluence determination [21] and were attached to the ^{13}C sample to form a stack of ^{197}Au -^{13}C- ^{197}Au. The uracil powder was pressed into pellets and similarly sandwiched between Au foils for the $^{14}N(n,p)$ studies.

In addition to the quasistellar neutron spectrum for $kT = 25$ keV produced at $E_p = 1912$ keV, spectra with an energy spread of ± 30 keV and mean energies of ~ 125 and ~ 180 keV were produced with the $^{7}Li(p,n)$ reaction at higher

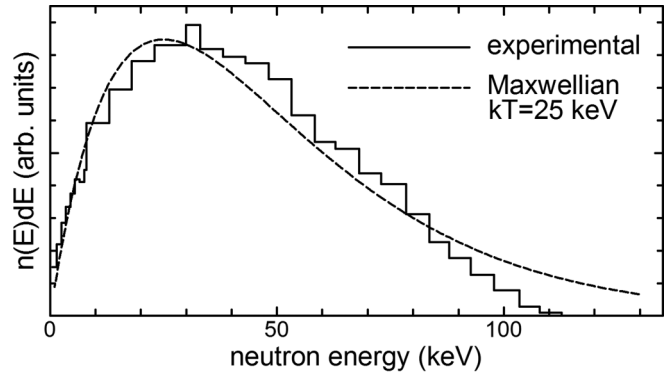

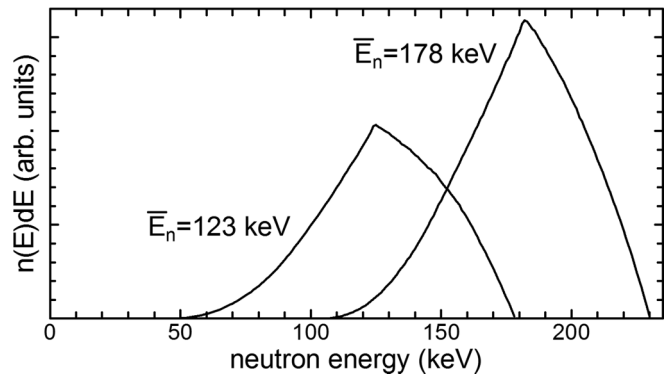

FIG. 4. Experimental neutron energy distributions used in the ^{14}N measurement. Apart from minor differences, the same spectra were applied in the ^{13}C runs (see Table II).

proton energies of 1960 and 2000 keV. With typical proton beam intensities of 100 μA, a fluence of $\sim 10^{15}$ neutrons per cm^2 could be obtained within five to seven days of activation (Table II). The neutron spectra obtained in this way have been calculated by means of the PINO code [22] (for details and individual data on the experimental neutron energy distributions, see Supplemental Material [23]).

The neutron spectra used in the irradiations are shown in Fig. 4. Although the ^{13}C and ^{14}N sandwich samples were irradiated simultaneously, the corresponding neutron spectra differ slightly because of small differences in their distance from the Li targets during the irradiations.

The main parameters for the Karlsruhe neutron activations are summarized in Table II. The applied neutron fluence for the

TABLE II. Main parameters for the neutron irradiations at the Karlsruhe VdG.

Reaction	Sample	Proton energy E_p (keV)	Mean neutron energy $\overline{E_n}$ (keV)	Gold cross section[a] (mb)	Neutron fluence[b] 10^{14} cm^{-2}
$^{13}C(n,\gamma)^{14}$	^{13}C Graphite-1	1912	25 (q-MB)	632 ± 9	13.8
	^{13}C Graphite-2	1960	128 ± 30	293 ± 6	6.65
	^{13}C Graphite-3	2000	182 ± 30	263 ± 5	4.67
$^{14}N(n,p)^{14}C$	Uracil-1	1912	25 (q-MB)	632 ± 9	8.04
	Uracil-2	1960	123 ± 30	299 ± 6	8.64
	Uracil-3	2000	178 ± 30	265 ± 5	6.04

[a]Spectrum averaged values.
[b]Systematic uncertainty ±3% (see Table VI).

various samples was determined from the induced activities of the gold monitor foils, using the ^{197}Au(n,γ) cross section as a reference.

The adopted gold reference cross section was taken from the new version KADONIS V1.0 [24]. Between $kT = 5$ and 50 keV it was derived by the weighted average of recent measurements at GELINA [25] and n_TOF [26,27] and between $kT = 60-100$ keV by the average of the evaluated cross sections from the data libraries JEFF-3.2, JENDL-4.0, ENDF/B-VII.1 [28–30]. This choice is in perfect agreement with a new activation measurement by the group in Sevilla [31]. The energy-differential gold cross section was folded with the neutron spectra used in these measurements. Note the effective values listed in column five of Table II are reflecting a change of 5.3% in the gold reference cross section compared to the values previously used in similar activation experiments.

V. ACCELERATOR MASS SPECTROMETRY

A. The VERA facility

AMS was introduced to laboratory experiments in nuclear astrophysics already in 1980 by Paul *et al.* [32] with a first study of the ^{25}Mg$(p,n)^{26}$Al reaction. In particular, the past few years have seen an increasing number of nuclear astrophysics measurements with the AMS technique for charged particle and neutron induced reactions (see, e.g., [33–41]).

Contrary to other mass spectrometric techniques AMS has the great advantage that it does not suffer from molecular interference effects, because molecules are completely destroyed in the gas stripper of the tandem accelerator. This method allows one even to separate specific atomic isobars, which can differ in their abundance ratios by many orders of magnitude. Therefore, AMS offers a highly sensitive and complementary tool for cross-section measurements of nuclear reactions leading to radioactive nuclides, independent of their half-lives or decay patterns. The list of reaction products of interest for astrophysics includes radioisotopes over the entire mass range, e.g., ^{10}Be, ^{14}C, ^{26}Al, ^{36}Cl, ^{41}Ca, ^{55,60}Fe, ^{59,63}Ni, ^{68}Ge, ^{79}Se, ^{129}I, ^{182}Hf, ^{202}Pb^{g}, ^{210}Bi^{m}, and a number of actinide isotopes including ^{244}Pu.

The present AMS measurements have been performed at the Vienna Environmental Research Accelerator (VERA) which represents a state-of-the-art AMS facility based on a 3-MV tandem [42,43]. A schematic view of the VERA facility is shown in Fig. 5 including the detection devices for recording the stable ^{12,13}C and the low-intensity ^{14}C ions.

B. AMS measurements

Both reactions under study are producing ^{14}C. Measurements of ^{14}C are commonly performed in most AMS laboratories, especially for ^{14}C dating. However, the samples from the neutron activations differ from routine measurements, because of the 10 000 times higher isotope ratio ^{13}C/^{12}C in the ^{13}C-enriched samples compared to natural material, where the ^{13}C abundance is only about 1%. Possible systematic uncertainties arising from the high enrichment have been studied with reference samples made from the original ^{13}C graphite that were activated at thermal energies. In this way,

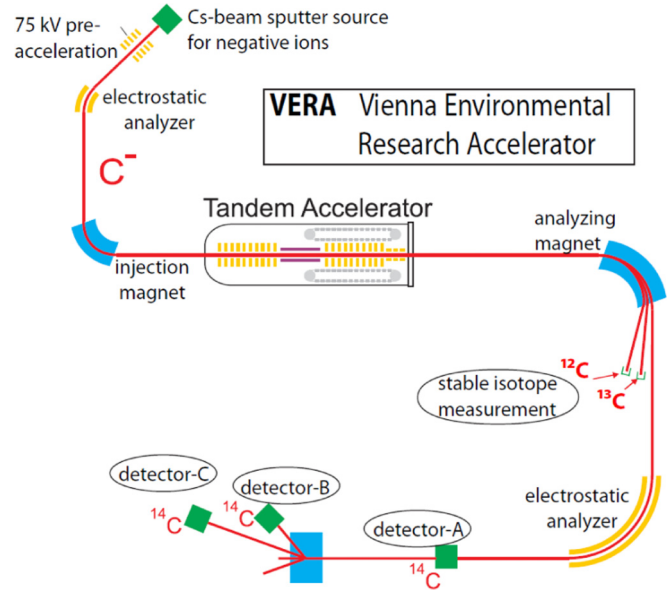

FIG. 5. Schematic layout of the AMS facility VERA. Negative ions (^{12,13,14}C^{-}) were extracted from the ion source and after low-energy mass analysis injected into the tandem accelerator. After gas stripping in the terminal and further acceleration, ions with charge 3^{+} and an energy of 12 MeV were selected with the analyzing magnet. The stable ^{12}C and ^{13}C ions were counted as current with Faraday cups, whereas the low-intensity ^{14}C fraction in the beam was subjected to further background suppression by the electrostatic analyzer and were eventually recorded with one of the energy detectors (A, B or C).

mass fractionation effects, which could lead to a systematic offset of the measured isotope ratio for such enriched materials, were excluded. These test runs were also used to study whether the highly enriched ^{13}C sample gave rise to an enhanced AMS background compared to measurements on natural graphite (which is assumed to be ^{14}C-free). It could be demonstrated that the amount of ^{14}C produced in the activations at keV neutron energies was high enough that this background did not jeopardize the final uncertainties [38,43,44].

The ^{13}C-enriched material used in this work was amorphous graphite powder. Prior to neutron irradiations the ^{14}C content of this material was determined with AMS. When the standard ^{14}C setup with particle detector A (Fig. 5) was used for analyzing the ^{13}C graphite and the uracil samples, it turned out that the ^{13}C-enriched graphite gave slightly enhanced ^{14}C count rates. The excess was interpreted as some leaky ^{13}C beam reaching the particle detector. Because these signals were indistinguishable from true ^{14}C events, two different particle detection systems further downstream were used instead, comprising an additional magnetic deflector and a multianode ionization chamber (detector B in Fig. 5) as well as a time-of-flight-detector (detector C). This enhanced setup gave stable isotope ratios ^{14}C/^{13}C $= (1 \pm 0.2) \times 10^{-14}$ for nonirradiated ^{13}C graphite (see Fig. 2 in [38]), corresponding to 48%, 11%, and 21% of the additional ^{14}C produced in the neutron irradiations at kT=25, 128, and 182 keV, respectively. Therefore, a series of nonirradiated blank samples

was measured in all beam times together with the irradiated samples to monitor the stability of the blank isotope ratios. The ^{14}C content in the blank samples contributed between 2% and 10% to the final uncertainties.

After the neutron irradiations the ^{13}C-enriched material was homogenized and a few mg were mixed with pure Ag powder as a binder and pressed into Al sample holders. A sample wheel with a capacity of 40 samples was then loaded into the sputter ion source of the AMS system.

Because of the low ^{14}C content in the ^{13}C-enriched samples, it was important to avoid contamination with natural carbon (with a $^{14}C/^{12}C$ ratio $\sim 10^{-12}$). Therefore, the stable carbon atom ratio $^{13}C/^{12}C$ was measured together with the $^{14}C/^{13}C$ ratio to monitor any such contamination. During the AMS runs the $^{13}C/^{12}C$ ratios were usually ranging between 10 and 70, thus any significant contamination with natural carbon could be excluded.

The ^{14}C content of unprocessed uracil was measured to $(1.8 \pm 1.0) \times 10^{-14}$, in agreement with the value measured with processed (graphitized) samples, which yielded $^{14}C/^{12}C$ ratios of $(1.4 \pm 0.5) \times 10^{-14}$. The irradiations of the uracil samples at Karlsruhe with keV neutrons generated isotope ratios $^{14}C/^{12}C$ of ~ 3–7×10^{-13}, much higher than the background contributions from the ^{14}C content of unprocessed uracil, the background in the AMS runs of $\sim 10^{-15}$, and a potential contamination with natural carbon during sample processing.

However, potential ^{14}C losses in the (n,p) reaction from outgassing of the reaction product ^{14}C could not be excluded *a priori*, because ^{14}C could potentially be released from the uracil matrix via recoil, subsequently forming gaseous ^{14}CO or $^{14}CO_2$. Uracil samples were irradiated at the TRIGA reactor in a thermal spectrum with an epithermal to thermal flux ratio of 1.3% [45] to study whether some of the freshly produced ^{14}C could be lost into the gas phase by conversion into ^{14}CO or $^{14}CO_2$.

The samples for these irradiations were prepared in different ways, by pressing uracil into pellets and by using the original powder in closed quartz ampoules. The latter form had the advantage that any gaseous ^{14}C could be extracted from the ampoules by separating it in a first step of the standard ^{14}C graphitization. After irradiation, AMS measurements were performed on unprocessed uracil, i.e., powder directly pressed into the AMS sample holders, as well as on uracil fully processed into graphite powder. The results demonstrated that outgassing of freshly produced ^{14}C from the uracil matrix was $\leqslant 2.5\%$ and compatible with ^{14}C production from ^{14}N in residual air in the quartz ampoules.

The AMS measurements were carried out with sub-mg pieces, taken randomly from the powderized uracil pellet. Although the pellets were thoroughly mixed after the irradiation, such small pieces were probably still not fully homogenized. Because of the close irradiation geometry of the pellet with respect to the neutron-producing Li target (pellet 6 mm in diameter, distance to target 2.57 mm), differences in the neutron flux of up to 30% might, in fact, be possible. This was reflected in the various runs, where differences up to 20% were found between the individual AMS samples of the same pellet. Therefore, between 11 and 14 sputter samples were measured from each pellet to balance the individual scatter. As the averaged isotope ratios did not show significant differences between unprocessed and processed sputter samples, it could be demonstrated that the final uncertainty was affected by $\leqslant 3\%$.

All samples (^{13}C graphite and uracil) were sputtered with a Cs beam and negative ions extracted from the ion source. An automated measurement procedure alternatively switched between the three different carbon isotopes (^{12,13,14}C) five times per second. The ion currents of the stable ^{12}C and ^{13}C were measured for milliseconds using Faraday cups at both, the low-energy side (before entering the accelerator, as $^{12,13}C^-$) and at the high-energy side (mass and charge selected ions after the analyzing magnet, as $^{12,13}C^{3+}$). The reaction product $^{14}C^{3+}$ was counted with the particle detection system for 95% of the sputtering time. Typical measuring times per such a run were about 200 s. Then another sample (unknown, blank or standard) was measured with the same setup. Typically, 5 to 10 runs were performed on each sample per measurement series, each series consisting of typically five sputter samples per neutron energy.

Overall, more than 200 AMS samples were measured in 6 and 10 beam times dedicated to the ^{13}C-enriched graphite and uracil samples, respectively. All measured isotope ratios were normalized to the principal modern radiocarbon standard oxalic acid I (NIST SRM 4990 B, also termed HOX-I) and oxalic acid II (HOX-II; NIST SRM 4990 C) [46,47]. This extensive body of data served to verify the reproducibility of the results and to reduce systematic backgrounds from the low isotope ratios in the irradiated samples. Statistical uncertainties were practically negligible in the final data.

VI. DATA ANALYSIS AND RESULTS

A. Neutron fluence

The neutron fluence applied during the irradiations is determined from the induced activity in the gold monitor foils, which was measured with a well-calibrated HPGe detector. The number of counts C in the characteristic 411.8-keV line in the γ-ray spectrum recorded during the measuring time t_m [20] is related to the number of activated nuclei A at the end of irradiation by

$$A = \frac{C}{K_\gamma \epsilon_\gamma I_\gamma (1 - e^{-\lambda t_m}) e^{-\lambda t_w}}, \tag{1}$$

where ϵ_γ denotes the detector efficiency, I_γ the intensity per decay, and t_w the waiting time between irradiation and activity measurement. The factor K_γ describes the γ-ray self-absorption in the sample, which is for the very thin gold disks in very good approximation [48],

$$K_\gamma = \frac{1 - e^{-\mu x}}{\mu x}, \tag{2}$$

where μ is the γ-ray self-absorption [49] and x the sample thickness.

The number of activated nuclei A can also be expressed by the neutron fluence $\Phi_{\text{tot}} = \int_0^{t_a} \Phi(t)dt$, the spectrum averaged capture cross section σ, and the sample thickness N in

atoms/cm^2 as

$$A = \Phi_{\rm tot} N \sigma f_b. \quad (3)$$

The fluence was determined from the activities of the Au monitor foils by folding the experimental neutron energy distributions (Ratynski and Käppeler distribution for 25 keV, and the simulated distributions around 125 and 180 keV) with the cross-section data for the ^{197}Au(n,γ) reaction.

The factor f_b in Eq. (3) corrects for the fraction of activated nuclei that decayed already during irradiation. By this correction nonuniformities in the neutron flux from the decreasing performance of the Li targets as well as fluctuations in the beam intensity were properly taken into account. This correction is small or negligible for activation products with half-lives much longer than the irradiation time t_a, but fluctuations in the neutron flux had to be considered for the gold activities, where the half-life of $t_{1/2} = 2.62$ d is shorter than the irradiation time. In the expression,

$$f_b = \frac{\int_0^{t_a} \Phi(t) e^{-\lambda(t_a - t)} dt}{\int_0^{t_a} \Phi(t) dt}, \quad (4)$$

$\Phi(t)$ is the time dependence of the neutron intensity recorded throughout the irradiation with the ^{6}Li glass monitor and λ the decay rate of the product nucleus ^{198}Au.

The main uncertainties in the fluence determination are from the gold reference cross section and the γ efficiency of the HPGe detector. The spectrum-averaged (n,γ) cross sections of ^{197}Au (Table II) are affected by uncertainties of 1.5%–2%. The γ efficiency was repeatedly measured with a set of calibrated sources and was known with an uncertainty of ±2.0%. All other uncertainties were very small and contribute less than 0.5% to the total 3% uncertainty of the neutron fluence.

B. Cross sections

1. ^{14}N$(n,p)^{14}$C

The experimental cross sections can simply be calculated from the following equation:

$$\sigma_{\rm exp} = \frac{^{14}{\rm C}}{^{14}{\rm N}} \times \frac{1}{\Phi_{\rm tot}}, \quad (5)$$

where ^{14}C/^{14}N denotes the isotope ratio measured via AMS, and $\Phi_{\rm tot}$ the neutron fluence discussed before. Note the particular advantage of the AMS method, i.e., that the cross section is determined by the measured isotope ratio only, completely independent of the sample mass and the decay properties of the product nucleus.

In fact, the measured isotope ratio for the ^{14}N$(n,p)^{14}$C reaction is ^{14}C/^{12}C, because ^{12}C is directly correlated with the number of ^{14}N atoms via the stoichiometry of the uracil compound $C_4H_4N_2O_2$ where ^{12}C/^{14}N=1.98 (99% ^{12}C, 1% ^{13}C).

The measured ^{14}C/^{12}C isotope ratios are listed in Table III together with the resulting spectrum averaged cross sections. Compared to typical experimental backgrounds in ^{14}C-AMS measurements (^{14}C/^{12}C $\sim 3 \times 10^{-16}$ for unprocessed and $\sim 10^{-15}$ for processed samples), it is obvious that machine backgrounds are not a critical issue for the uncertainty budget. The systematic uncertainties are summarized in Table VI.

TABLE III. Measured isotope ratios and spectrum-averaged cross sections for ^{14}N(n,p).

E_n (keV)	No. of sputter samples	^{14}C/^{12}C ($\times 10^{-13}$)	$\sigma(^{14}$N(n,p) (mb)
Blank	24	0.16 ± 0.05	
⟨25⟩ (q-MB)	14	6.90 ± 0.35	1.74 ± 0.10
123 ± 30	12	3.73 ± 0.19	0.88 ± 0.05
178 ± 30	10	2.51 ± 0.13	0.90 ± 0.05

The new spectrum-averaged cross-section data for ^{14}N(n,p) (full squares) are plotted in Figure 6 together with previous experimental data and with the JEFF-3.2 evaluation [50]. At 25 keV there is perfect agreement with the work of Sanami *et al.* [16]. Up to about 100 keV all data are well consistent with a 1/v shape of the cross section. The only exception are the values of Brehm *et al.* [13], which should be rejected in further evaluations.

A best-fit cross section was obtained via

$$\sigma(E_n) = \sigma_{1/{\rm v}} + \sigma_{\rm R}, \quad (6)$$

following the prescription of the JEFF 3.2 evaluation [50], where the first term corresponds to the 1/v extrapolation of the thermal cross section (1860 ± 30 mb [19]) and the second term considers the tails of the resonances at 493 keV and above. The best-fit cross section (solid line in Fig. 6) was obtained by adopting the well-confirmed 1/v trend below about 25 keV, the resonance contribution was modified to match our data points at 123 and 178 keV. This implies that the strength of the resonance at $E_n = 493$ keV reported in [51] had to be reduced by a factor of 3.3, resulting in significantly lower cross sections than in JEFF-3.2. Folded with the neutron energy spectra of this work, all experimental results are well reproduced by the best-fit cross section as indicated by open boxes in Fig. 6. The width of the boxes corresponds to the full width at half maximum (FWHM) of the respective neutron spectra.

2. ^{13}C$(n,\gamma)^{14}$C

In the analysis of the ^{13}C(n,γ) cross section the measured ^{14}C/^{13}C ratios had to be corrected for parasitic ^{14}C production via ^{14}N(n,p) from a nitrogen contamination of

TABLE IV. Measured effective cross sections for ^{13}C(n,γ) and ^{14}N(n,p) and background from the ^{14}N contamination[a].

Neutron energy	^{13}C(n,γ) (μb)	^{14}N(n,p) (mb)	$\sigma_{np}/\sigma_{n\gamma}$	background from ^{14}N(n,p) (in %)
Thermal[b]	1370 ± 40	1860 ± 30	1358	666 ± 65
25 (q-MB)[c]	6.7	1.74	260	127 ± 13
125 ± 30 keV	136	0.88	6.5	3.2 ± 0.3
180 ± 30 keV	99	0.90	9.1	4.5 ± 0.5

[a]For a content of ^{14}N/^{13}C = 0.49 ± 0.04% (Sec. VI B 2).
[b]Ref. [19].
[c]Quasi-Maxwell-Boltzmann distribution for $kT = 25$ keV (Sec. IV).

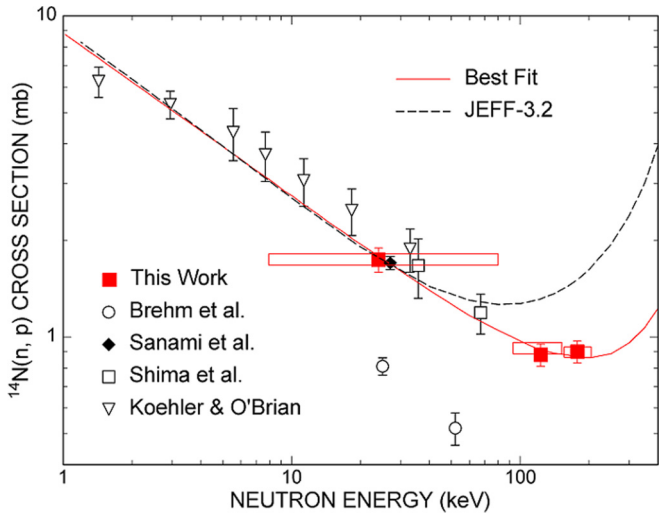

FIG. 6. The $^{14}N(n,p)^{14}C$ cross section between 1 and 400 keV. The plot shows a comparison of the present results (full squares) with existing experimental data [13–16] and with the evaluated cross section in the JEFF-3.2 library [50]. In general, there is very good agreement with existing data except for the values of Brehm *et al.* [13]. The solid line represents a best-fit cross section, yielding average values (FWHM indicated by open boxes) in good agreement with the experimental results.

the enriched ^{13}C material. (Interestingly, the ^{14}N content in natural graphite was below the detection limit of <0.01%). The total number of produced ^{14}C atoms is

$$N_{^{14}C} = (\sigma_{13C} \times N_{13C} + \sigma_{14N} \times N_{14N})\phi_n, \quad (7)$$

where σ_{13C} and σ_{14N} denote the $^{13}C(n,\gamma)$ and $^{14}N(n,p)$ cross sections and N_{13C} and N_{14N} are the number of ^{13}C and ^{14}N atoms in the sample, respectively. With

$$\sigma_{prod} = \sigma_{13C} + \sigma_{14N} = (^{14}C/^{13}C)_{AMS} \times 1/\phi,$$

one gets

$$\frac{N_{14N}}{N_{13C}} = \left(\frac{\sigma_{prod}}{\sigma_{13C}} - 1\right) \times \left(\frac{\sigma_{13C}}{\sigma_{14N}}\right). \quad (8)$$

The thermal cross section of $^{13}C(n,\gamma)^{14}C$ is 1.37 ± 0.04 mb [19]. This means that (9.1 ± 0.6) mb out of the measured $\sigma_{prod} = 10.5$ mb (Table I) are from $^{14}N(n,p)$ reactions in the sample. From the measured σ_{prod} and the thermal cross-section ratio (Table IV) one finds an isotope ratio of $^{14}N/^{13}C = 0.0049 \pm 0.0004$, in full agreement with the direct AMS result of 0.005 ± 0.001.

Eventually, the $^{13}C(n,\gamma)$ cross section can be expressed as

$$\sigma_{13C} = \sigma_{prod} - \sigma_{14N} \times \frac{N_{14N}}{N_{13C}}. \quad (9)$$

The correction for the amount of ^{14}C from the ^{14}N contamination of the ^{13}C-enriched samples was determined using the measured cross-section values for $^{14}N(n,p)$ described above. At $kT = 25$ keV, the parasitic $^{14}N(n,p)$ component was even larger than ^{14}C generated from the $^{13}C(n,\gamma)$ reaction and it contributed about 43% to the final uncertainty. At the higher neutron energies of 128 and 182 keV the corrections were only 3.2 and 4.5%, respectively.

TABLE V. Measured isotope ratios, effective spectrum-averaged cross sections, and corrected net cross sections, $\langle\sigma\rangle$, for the $^{13}C(n,\gamma)^{14}C$ reaction.

E_n (keV)	$^{14}C/^{13}C$ ($\times 10^{-15}$)	σ_{prod} (μb)	$\langle\sigma\rangle$ (μb)
Blank	10 ± 2		
$\langle 25\rangle$ (q-MB)	21 ± 4	15.2 ± 2.9	6.7 ± 3.2
128 ± 30	93 ± 7	140 ± 11	136 ± 11
182 ± 30	48 ± 5	103 ± 10	99 ± 12

The measured $^{14}C/^{13}C$ isotope ratios and the resulting cross sections for the $^{13}C(n,\gamma)^{14}C$ reaction are listed in Table V and the related systematic uncertainties are summarized in Table VI.

The present results for the $^{13}C(n,\gamma)^{14}C$ cross section are plotted in Fig. 7 together with previous experimental results [7,8], and with the evaluated data from the JEFF-3.2 library [28]. A best fit to the present data (solid line) was obtained following the prescription of Herndl *et al.* [9], that considered the effect of the direct radiative capture (DRC) channel in detail. To reproduce the data points at 128 and 182 keV it was particularly important that also the *p*- and *d*-wave DRC components were considered including a constructive interference between the *p*-wave part and the 152.4-keV resonance by this approach.

The best fit was obtained with the expression,

$$\sigma(E_n) = \sigma_R + \sigma^s_{DRC} + \sigma^p_{DRC} + \sigma^d_{DRC} \pm 2\sqrt{\sigma_R \sigma^p_{DRC}}\cos[\delta(E_n)], \quad (10)$$

where σ_R denotes the resonant part described by the usual Breit-Wigner form with the resonance parameters taken from Ref. [19], except that the capture width was increased by 60% to $\Gamma_\gamma = 0.35$ eV for matching the data points at 128 and 182 keV. The *s*-wave DRC component σ^s_{DRC} is represented

TABLE VI. Major systematic uncertainties of averaged cross sections (in %).

Source of uncertainty	$^{13}C(n,\gamma)^{14}C$	$^{14}N(n,p)^{14}C$
Neutron fluence		
Gold cross section	1.5/2.0/2.0[a]	1.5/2.0/2.0[b]
Counting efficiency	2.0	2.0
γ intensity per decay	<0.5	<0.5
Time factors	<0.5	<0.5
AMS measurement		
Flux anisotropy	3.0	3.0
^{14}N-induced background	43/0.3/0.5[a]	
^{14}C in sample material	19/7 /10[a]	3.0
^{14}C in blank samples	10/2/4[a]	2.0
Total	48/8/12[a]	6/6/6[b]

[a]For neutron energies 25 (q-MB), 128, and 182 keV.
[b]For neutron energies 25 (q-MB), 123, and 178 keV.

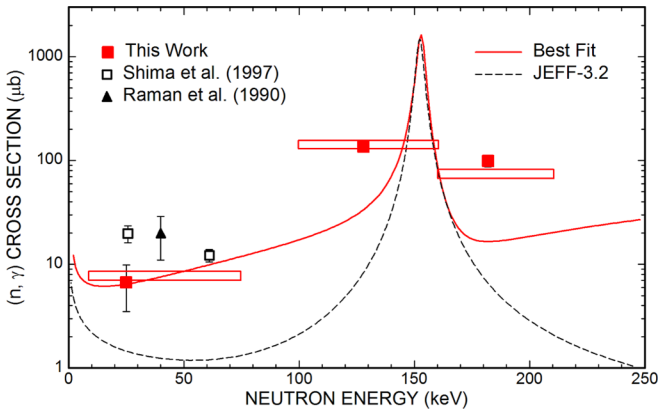

FIG. 7. The $^{13}C(n,\gamma)^{14}C$ cross section between 1 and 300 keV. The solid line represents a best-fit cross section obtained with the prescription described in the text. Folded with the neutron energy spectra of this work, this best fit yields average values (open boxes indicating the FWHM) in good agreement with the experimental results. Because the p- and d-wave components of the DRC contribution were neglected in the evaluation, the JEFF 3.2 cross section (dashed line) is too small in the astrophysically relevant region below the resonance at 152.4 keV.

by a 1/v extrapolation of the thermal cross section [19], and the d-wave part was adopted from the work of Herndl *et al.* [9]. The last term describes the interference between the p-wave DRC component and the resonant part, which changes sign at the resonance. The phase shift $\delta(E_n)$ is given by

$$\delta(E_n) = \arctan \frac{\Gamma}{2(E_n - E_0)}.$$

The p-wave component, which is characterized by an $\sqrt{E_n}$ energy dependence, was then adjusted to best reproduce the experimental data at 128 and 182 keV.

In this way it was possible to reproduce the data points at 128 and 182 keV within the respective uncertainties, in contrast to attempts neglecting the interference term. At 25 keV, the situation remains ambiguous because the present data point is somewhat uncertain because of the large correction for the ^{14}N contamination of the sample. Lower than previous data [7,8], the fit matches the measured cross section well within the 1σ uncertainty as shown in Fig. 7. The importance of the p- and d-wave DRC components is illustrated by comparison of the best fit with the recent JEFF-3.2 evaluation [28], where these components had been neglected (dashed line). The evaluation is significantly underestimating the measured cross section, particularly in the astrophysically relevant region below the resonance at 152.4 keV.

VII. MAXWELLIAN AVERAGED CROSS SECTIONS

Maxwellian averaged cross sections (MACS) for $kT = 5$–100 keV have been calculated using the best-fit cross sections to the measured data as indicated by the solid lines in Figs. 6 and 7. The MACS values for both reactions are listed in Table VII.

TABLE VII. Maxwellian average cross sections compared to values recommended in KADONIS [12].

kT	$^{13}C(n,\gamma)^{14}C$ (μb)		$^{14}N(n,p)^{14}C$ (mb)
(keV)	This work	KADONIS	This work
5	8.3 ± 1.1	5.9	3.78 ± 0.06
8	8.1 ± 1.0		3.12 ± 0.05
10	8.2 ± 1.4	6.4	2.89 ± 0.05
15	9.6 ± 1.7	7.5	2.47 ± 0.04
20	13.8 ± 2.3	10	2.21 ± 0.04
23	17.6 ± 2.5		2.09 ± 0.04
25	20.6 ± 2.7	15	2.03 ± 0.04
30	28.7 ± 3.0	21 ± 4	1.93 ± 0.04
40	43.7 ± 4.9	32	1.85 ± 0.05
50	54.0 ± 6.1	40	1.83 ± 0.06
60	60.1 ± 6.9	45	1.84 ± 0.07
80	65.0 ± 7.9	49	1.84 ± 0.08
100	65.7 ± 8.4	50	1.83 ± 0.08

For the $^{14}N(n,p)$ reaction, the 1.6% uncertainty of the thermal value was adopted for the 1/v term. As the resonant part is firmly constrained by the measured cross sections at 123 and 178 keV, the 6% uncertainty of these data points was assigned to this component. Accordingly, the respective MACS uncertainties correspond to the relative contributions of the two terms in Eq. (6).

Compared to the MACS data calculated with the JEFF 3.2 evaluation of the $^{14}N(n,p)$ cross section [50], the new values are lower by 1%, 11%, and 100% at thermal energies of 10, 25, and 100 keV, respectively.

The uncertainties of the MACS calculation for the $^{13}C(n,\gamma)$ reaction had to consider all terms in Eq. (10). For the resonant part σ_R, an uncertainty of 9% was considered, corresponding the uncertainties of the data points at 128 and 182 keV, which are constraining the resonant part. As the s-wave DRC component was normalized via the thermal cross section, the 1% uncertainty of this value [19] was adopted for this modest contribution. To accommodate the existing experimental values below 60 keV, a conservative uncertainty of 30% was assigned to the p-wave DRC component. For the d-wave DRC component, which contributes mostly above the 152.4-keV resonance, an uncertainty of 20% was estimated for the adopted DRC calculation of Herndl *et al.* [9].

For thermal energies up to 20 keV the present MACS values for ^{13}C and the recommended values in KADONIS [12] are compatible within uncertainties. However, above $kT \geqslant 25$ keV the new data are consistently higher because (i) the constructive interference between the 152-keV resonance and the p-wave DRC component and (ii) the effect of the previously neglected d-wave DRC contribution.

The present MACS results are compared in Fig. 8 with data obtained from the evaluated cross sections in the JEFF-3.2 library [50]. As expected from the respective cross sections in Figs. 6 and 7 the $^{14}N(n,p)^{14}C$ values exhibit good agreement up to $kT = 30$ keV and start to exceed the new values at higher thermal energies, whereas the JEFF-3.2 points for $^{13}C(n,\gamma)^{14}C$ are lower by factors of 2–4, mostly because the contributions

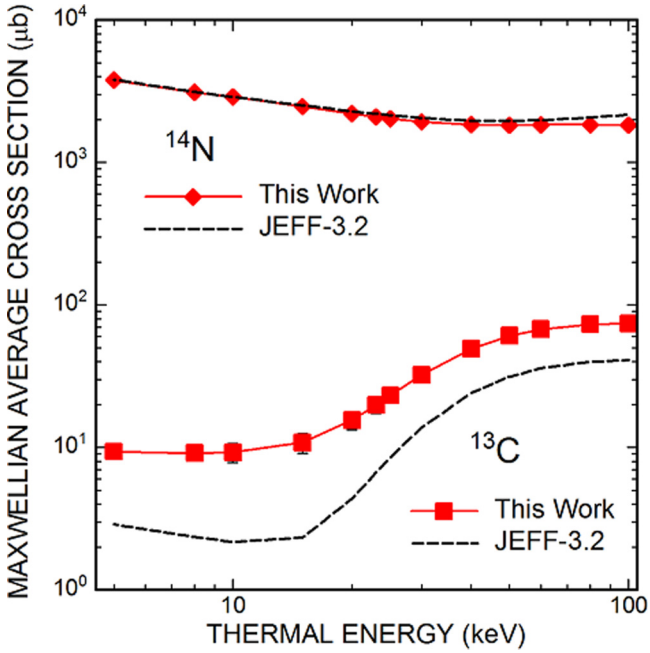

FIG. 8. Comparison of the present MACS results with data obtained from the evaluated cross sections in the JEFF-3.2 library [50].

of the *p*-and *d*-wave DC components were neglected in the evaluated cross section.

VIII. IMPACT FOR *s*-PROCESS CALCULATIONS

We investigated the effect of the new stellar cross sections on the *s* process in low-mass AGB stars using stellar models of initial mass 2 $M_\odot$ and two different metallicities: solar ($Z=0.014$) and roughly 1/10th of solar ($Z=0.001$). The nucleosynthesis post-processing code includes a nuclear network up to Po and is fed with the results from evolutionary sequences computed using the MONASH/MT STROMLO evolutionary code [52] in terms of temperatures, densities, convective velocities, and locations of the convective borders at each time and point in the star. Detailed information about the stellar evolutionary sequences can be found in [53] and [54]. The numerical method used in this study was described by Lugaro *et al.* [55].

During the post-processing we artificially included a proton profile in the He-rich intershell at the deepest extent of each dredge-up episode (as schematically illustrated in Fig. 1). The proton abundance is chosen such that it decreases exponentially from the envelope value ∼0.7 to a value of 10^{-4} at a location in mass 2×10^{-3} $M_\odot$ below the base of the envelope. A thin region forms as a result of such mixing, which is rich in ^{13}C in the bottom layers and in ^{14}N in the top layer. We run all the tests with the same input for the stellar and the nuclear physics (mixing, rates, initial abundances, etc.), except that we modified the rates of the ^{13}C$(n,\gamma)^{14}$C and the ^{14}N$(n,p)^{14}$C reactions to those reported here. We compare the results to those obtained using the ^{13}C$(n,\gamma)^{14}$C rate from the KADONIS database and the ^{14}N$(n,p)^{14}$C rate from Caughlan and Fowler (1980), which are the recommended rates in the JINA reaclib database that we employ as the standard in our models. The ^{14}N(n,p) rate from Caughlan and Fowler [56] is roughly 20% higher than the rate reported here and close to the evaluation by Koehler and O'Brien [14].

Changing the ^{13}C(n,γ) rate alone did not make any difference in the final results. Changing the ^{14}N(n,p) rate alone resulted in a small increase (by 15% at most in the Z=0.014 model and by 4% at most in the $Z=0.001$ model) in the amount of Ba and Pb produced. This was expected as the new rate is lower than the previous, which results in a higher number of free neutrons in the ^{13}C pocket and a higher production of the heavier *s*-process elements. When we changed both rates to the new values the effect was slightly strengthened in the low-metallicity model (up to a 9% increase in Ba) because of the feedback between the two reactions.

We also experimented with a model of a 1.25 $M_\odot$ star with Z=0.01, where the third dredge-up was calculated using overshoot (see details in [57]). In this case the ^{13}C pocket is artificially included as in the other models, however, because the temperature in that region only reaches up to 70 MK before the onset of the following thermal instability, the ^{13}C(α,n) ^{16}O reaction is not activated until the ^{13}C nuclei are ingested in the following convective region [58]. In this case the impact of the ^{14}N$(n,p)^{14}$C neutron poison reaction is even more crucial because the large amount of ^{14}N present in the H-burning ashes is ingested at the same time. The total number of free neutrons is much lower than in the 2 $M_\odot$ models and the production of the elements belonging to the first, rather than the second and third, *s*-process peak is favored. In any case, also in this model the new rates produce marginal changes (an increase of 16% in Ba).

Overall there are no major differences between the different sets of models, especially in relation to observational counterparts such as data from spectroscopic observations and meteoritic stardust grains, whose determinations have larger uncertainties than the differences found here. The present rates allow us to confirm the accuracy of the current *s*-process results in relation to the behavior of these two fundamental reactions.

IX. SUMMARY

Over the past decade AMS measurements have provided data for open questions in nuclear astrophysics. In the present work we exemplified this technique via measurements of the ^{13}C(n,γ) and ^{14}N(n,p) reaction cross sections. Samples containing ^{13}C and ^{14}N were irradiated at the Karlsruhe Van de Graaff accelerator in a neutron field with the proper energy distribution for the direct determination of a Maxwellian-averaged cross section at 25-keV thermal energy, and also with broad neutron energy distributions of $E_n=123$ and 178 keV mean energy. After neutron activation the amount of ^{14}C produced was quantitatively determined by AMS. ^{13}C$(n,\gamma)^{14}$C and ^{14}N$(n,p)^{14}$C reactions act both as neutron poisons in *s*-process nucleosynthesis, while ^{14}N(n,p) also serves as a proton donator, leading to a delayed neutron recycling. The protons released in this reaction are as well important for the production of ^{19}F.

The measured ^{13}C(n,γ) cross section at $kT=25$ keV was found to be significantly smaller than previous results. With

the data points at 128 and 182 keV neutron energy, the strength of the resonance at 143 keV could be constrained for the first time. Together with a more rigorous treatment of the direct radiative capture (DRC) channels [9], this resulted in much improved MACS data above $kT = 20$ keV. The $^{14}\mathrm{N}(n,p)^{14}\mathrm{C}$ cross section was measured at similar neutron energies, in a quasistellar spectrum for $kT = 25$ keV and at 123 and 178 keV. Also in this case, the contributions of resonances at 493 keV and above could be constrained, yielding reduced MACS values by 1%, 11%, and 100% at $kT = 10$, 25, and 100 keV, respectively.

The impact of the new MACS data on the *s*-process abundance distribution is somewhat modest. Abundances are found to change by less than 20% for different sets of models, smaller than the intrinsic uncertainties of observational counterparts such as data from spectroscopic observations and meteoritic stardust grains. Accordingly, the present rates allow us to confirm the accuracy of the current *s*-process results.

ACKNOWLEDGMENTS

This work was partly funded by the Austrian Science Fund (FWF), Projects No. P20434 and No. I428-N16, and by the Australian Research Council (ARC), Project No. DP140100136.

[1] F. Käppeler, R. Gallino, S. Bisterzo, and W. Aoki, Rev. Mod. Phys. **83**, 157 (2011).
[2] R. Reifarth, C. Lederer, and F. Käppeler, J. Phys. G: Nucl. Part. Phys. **41**, 053101 (2014).
[3] R. Gallino *et al.*, Ap. J. **497**, 388 (1998).
[4] F. Herwig, Ap. J. **605**, 425 (2004).
[5] O. Straniero, S. Cristallo, and R. Gallino, Publ. Astron. Soc. Australia **26**, 133 (2009).
[6] O. Trippella *et al.*, Ap. J. **787**, 41 (2014).
[7] S. Raman, M. Igashira, Y. Dozono, H. Kitazawa, M. Mizumoto, and J. E. Lynn, Phys. Rev. C **41**, 458 (1990).
[8] T. Shima *et al.*, Nucl. Phys. A **621**, 231c (1997).
[9] H. Herndl, R. Hofinger, J. Jank, H. Oberhummer, J. Görres, M. Wiescher, F. K. Thielemann, and B. A. Brown, Phys. Rev. C **60**, 064614 (1999).
[10] *Nuclear Physics of Stars*, edited by C. Iliadis (Wiley-VCH Verlag, Weinheim, 2007), p. 518.
[11] Z. Bao *et al.*, At. Data Nucl. Data Tables **76**, 70 (2000).
[12] I. Dillmann, R. Plag, F. Käppeler, and T. Rauscher, in *EFNUDAT Fast Neutrons, Sci. Workshop on Neutron Measurements, Theory, and Applications*, edited by F.-J. Hambsch (Publications Office of the European Union, Luxembourg, 2010), pp. 55–58.
[13] K. Brehm *et al.*, Z. Phys. A **330**, 167 (1988).
[14] P. E. Koehler and H. A. O'Brien, Phys. Rev. C **39**, 1655 (1989).
[15] T. Shima, K. Watanabe, T. Irie, H. Sato, and Y. Nagai, Nucl. Instr. Meth. A **356**, 347 (1995).
[16] T. Sanami *et al.*, Nucl. Instr. Meth. A **394**, 368 (1997).
[17] M. Lugaro *et al.*, Ap. J. **615**, 934 (2004).
[18] M. Lugaro *et al.*, Astron. Astrophys. **484**, L27 (2008).
[19] S. Mughabghab, *Atlas of Neutron Resonances*, 5th ed. (Elsevier, Amsterdam, 2006).
[20] H. Beer and F. Käppeler, Phys. Rev. C **21**, 534 (1980).
[21] W. Ratynski and F. Käppeler, Phys. Rev. C **37**, 595 (1988).
[22] R. Reifarth, M. Heil, F. Käppeler, and R. Plag, Nucl. Instr. Meth. A **608**, 139 (2009).
[23] See Supplemental Material at http://link.aps.org/supplemental/10.1103/PhysRevC.93.045803 for individual data on the experimental neutron energy distributions.
[24] I. Dillmann *et al.*, Nucl. Data Sheets **120**, 171 (2014).
[25] C. Massimi *et al.*, Eur. Phys. J. A **50**, 124 (2014).
[26] C. Massimi *et al.*, Phys. Rev. C **81**, 044616 (2010).
[27] C. Lederer *et al.*, Phys. Rev. C **83**, 034608 (2011).
[28] A. Koning and D. Rochman, Nucl. Data Sheets **113**, 2841 (2012).
[29] K. Shibata *et al.*, J. Nucl. Sci. Technol. **48**, 1 (2011).
[30] M. Chadwick *et al.*, Nucl. Data Sheets. **112**, 2887 (2011).
[31] P. Jiménez-Bonilla and J. Praena, in *Proceedings of Science, Nuclei in the Cosmos XIII_102* (SISSA, Trieste, 2014).
[32] M. Paul *et al.*, Phys. Lett. B **94**, 303 (1980).
[33] M. Paul *et al.*, Nucl. Phys. A **718**, 239 (2003).
[34] H. Nassar, M. Paul, I. Ahmad, Y. Ben-Dov, J. Caggiano, S. Ghelberg, S. Goriely, J. P. Greene, M. Hass, A. Heger, A. Heinz, D. J. Henderson, R. V. F. Janssens, C. L. Jiang, Y. Kashiv, B. S. Nara Singh, A. Ofan, R. C. Pardo, T. Pennington, K. E. Rehm, G. Savard, R. Scott, and R. Vondrasek, Phys. Rev. Lett. **96**, 041102 (2006).
[35] A. Arazi, T. Faestermann, J. O. Fernández Niello, K. Knie, G. Korschinek, M. Poutivtsev, E. Richter, G. Rugel, and A. Wallner, Phys. Rev. C **74**, 025802 (2006).
[36] H. Nassar, M. Paul, I. Ahmad, D. Berkovits, M. Bettan, P. Collon, S. Dababneh, S. Ghelberg, J. P. Greene, A. Heger, M. Heil, D. J. Henderson, C. L. Jiang, F. Kappeler, H. Koivisto, S. OBrien, R. C. Pardo, N. Patronis, T. Pennington, R. Plag, K. E. Rehm, R. Reifarth, R. Scott, S. Sinha, X. Tang, and R. Vondrasek, Phys. Rev. Lett. **94**, 092504 (2005).
[37] A. Wallner *et al.*, Nucl. Instr. Meth. B **259**, 677 (2007).
[38] A. Wallner, Nucl. Instr. Meth B **268**, 1277 (2010).
[39] I. Dillmann *et al.*, Nucl. Instr. Meth. B **268**, 1283 (2010).
[40] G. Rugel *et al.*, Nucl. Inst. Meth. B **259**, 683 (2007).
[41] A. Wallner *et al.*, Phys. Rev. Lett. **112**, 192501 (2014).
[42] P. Steier *et al.*, Nucl. Instr. Meth. B **240**, 445 (2005).
[43] A. Wallner *et al.*, Pub. Astron. Soc. Aust. **29**, 115 (2012).
[44] A. Wallner *et al.*, J. Phys. G: Nucl. Part. Phys. **35**, 014018 (2008).
[45] C. Vockenhuber, M. Bichler, A. Wallner, W. Kutschera, I. Dillmann, and F. Kappeler, Phys. Rev. C **77**, 044608 (2008).
[46] W. B. Mann, Radiocarbon **25**, 519 (1983).
[47] R. J. Schneider *et al.*, Radiocarbon **37**, 693 (1995).
[48] W. Dixon, Nucleonics **8**, 68 (1951).
[49] J. H. Hubbell and S. M. Seltzer, *Tables of X-Ray Mass Attenuation Coefficients and Mass Energy-Absorption Coefficients (version 1.4)* (National Institute of Standards and Technology, Gaithersburg, MD, 2004), http://physics.nist.gov/xaamdi.
[50] M. Chadwick, P. Young, G. M. Hale *et al.*, *Technical Report No. LA-UR-99-1222* (Los Alamos National Laboratory, Los Alamos, 1999).
[51] G. L. Morgan, Nucl. Sci. Eng. **70**, 163 (1979).
[52] J. Lattanzio, Ap. J. **311**, 708 (1986).

[53] A. Karakas and J. Lattanzio, Publ. Astron. Soc. Australia **31**, e030 (2014).
[54] C. Fishlock, A. Karakas, M. Lugaro, and D. Yong, Ap. J. **797**, 44 (2014).
[55] M. Lugaro, A. Karakas, R. Stancliffe, and C. Rijs, Ap. J. **747**, 2 (2012).
[56] G. Caughlan and W. Fowler, Atomic Data Nucl. Data Tables **40**, 283 (1988).
[57] A. Karakas, Mon. Not. R. Astron. Soc. **403**, 1413 (2010).
[58] M. Lugaro, G. Tagliente, A. I. Karakas, P. M. Milazzo, F. Käppeler, A. M. Davis, and M. R. Savina, Ap. J. **780**, 95 (2014).